Available online at www.sciencedirect.com

jmr&t Journal of Materials Research and Technology

journal homepage: www.elsevier.com/locate/jmrt

Original Article

# Decomposition of γ-Fe in 0.4C–1.8Si-2.8Mn-0.5Al steel during a continuous cooling process: A comparative study using in-situ HT-LSCM, DSC and dilatometry

*Man Liu* [a,c], *Michael Bernhard* [b,c,*], *Monika Kawuloková* [d], *Josef Walek* [e], *Maximilian Kern* [b], *Simona Zlá* [d], *Peter Presoly* [b], *Bedrich Smetana* [d], *Marketa Tkadlečková* [e], *Guang Xu* [a], *Youn-Bae Kang* [b], *Christian Bernhard* [b]

[a] *The State Key Laboratory of Refractories and Metallurgy, The Collaborative Innovation Center for Advanced Steels of Ministry of Education, The Key Laboratory for Ferrous Metallurgy and Resources Utilization of Ministry of Education, Wuhan University of Science and Technology, Wuhan, 430081, China*

[b] *Graduate Institute of Ferrous and Energy Materials Technology, Pohang University of Science and Technology, 77, Cheongam-ro, Nam-gu, Pohang-si, Gyeongsangbuk-do, Republic of Korea*

[c] *Chair of Ferrous Metallurgy, Montanuniversitaet Leoben, Franz-Josef-Strasse 18, 8700, Leoben, Austria*

[d] *Department of Chemistry and Physico-Chemical Processes, Faculty of Materials Science and Technology, VSB-Technical University of Ostrava, 17. Listopadu 2172/15, 70800, Ostrava, Czech Republic*

[e] *Department of Metallurgical Technologies, Faculty of Materials Science and Technology, VSB-Technical University of Ostrava, 17. Listopadu 2172/15, 70800, Ostrava, Czech Republic*

ARTICLE INFO

*Article history:*
Received 6 March 2023
Accepted 1 April 2023
Available online 7 April 2023

*Keywords:*
Thermal analysis
HT-LSCM
Dilatometry
DSC
CCT
Heat treatment

ABSTRACT

Continuous cooling transformation (CCT) diagrams represent roadmaps for producing all heat-treatable steels. CCT curves provide valuable information on the solid-state phase transformation sequence, depending on the defined cooling strategies, the alloying concept of the steel and previous processing steps. The experimental characterization of CCT diagrams is usually done on a laboratory scale applying thermal analysis of dilatometry. In current research studies, however, also other in-situ methods such as high-temperature laser scanning confocal microscopy (HT-LSCM) or differential scanning calorimetry (DSC) are frequently used to investigate phase transformations during thermal cycling. In the present study, HT-LSCM observations and DSC analysis are critically compared with dilatometry results by investigating the CCT diagram of a 0.4%C-1.8%Si-2.8%Mn-0.5%Al (in mass pct.) advanced steel grade. Furthermore, classical examinations by optical microscopy and hardness measurements were performed to support the analysis. In general, very good consistencies between all experimental techniques were identified in determining the transformation start temperature for pearlite, bainite and martensite. The optical microscopy confirmed the observed phase transformations and the results

* Corresponding author.
E-mail address: michael.bernhard@unileoben.ac.at (M. Bernhard).
https://doi.org/10.1016/j.jmrt.2023.04.009

correlated with the measured hardness response. Based on the results, coupling of HT-LSCM and DSC is considered as a valuable novel approach to plot CCT diagrams in future research.



## 1. Introduction

In continuous cooling transformation (CCT) diagrams, fundamental processing parameters, e.g., cooling rate, are graphically linked to the final microstructure and corresponding hardness of quenched steels, fully annealed steels or the heat-affected zone in steel welding [1,2]. During the supercooling of austenite, phase transformations depend on the chemical composition of the steel [3,4], the extent of austenite homogenizing [1], the austenite grain size (AGS), and the austenitizing temperature and time [5,6]. Currently, CCT diagrams are obtained either from directly plotting the experimental data or from semi-empirical equations using the chemical composition of the steel and its austenitizing treatments as input values. Many attempts have been undertaken at modeling austenite transformations in steel during cooling [7–10]. The calculation methods provide a valuable alternative to experimental measurement in predicting the material data required for heat treatment simulation. However, the calculation results strongly depend on the quality and amount of the experimental data used in adjusting the model parameters.

Thermal analysis by dilatometry is widely utilized to determine transformation temperatures in CCT diagrams. The measured dilatation is plotted over temperature and the tangent method is applied to characterize the inflection points of dilation curves, which represent the transformation temperatures due to the different expansion coefficients of $\gamma$ and $\alpha$ phases [11,12]. The cooling rate region of 0.08–44 °C $s^{-1}$ was designed to obtain static CCT curves of bainitic forging steels [13]. The dynamic CCT curves of three CrMoV steels with cooling rates between 5 and 100 °C $s^{-1}$ were plotted by Siwecki et al. [14]. The CCT diagrams of medium carbon steels with different Cr, V, Ti and Mn contents [15], low-carbon boron steels [16], linepipe steel [17] and additive manufacturing deposited steels [18] could be measured successfully and drawn through dilatometry.

Differential scanning calorimetry (DSC) analysis represents another effective method to measure the transformation temperatures according to the change in heat flow [19]. Ganesh et al. [20] designed the cooling rate range of 0.017–0.05 °C $s^{-1}$ to measure the martensite starting temperature of low-carbon 9Cr steels with the help of DSC. Additionally, high temperature-laser scanning confocal microscopy (HT-LSCM) was utilized to directly and dynamically observe the nucleation of ferrite, bainite and martensite at different cooling rates [21]. The CCT diagram with a cooling rate from 0.50 to 8 °C $s^{-1}$ of a 0.14 mass pct. C microalloyed steel was obtained by HT-LSCM [22]. Hence, this technique provides another valuable option to draw the CCT diagram based on the thermally etched microstructure.

Recently, the coupling of two selected *in-situ* methods mentioned above has been reported in the literature. Dilatometry and DSC analyses were used by Xu et al. [23] to plot the CCT diagram of medium-carbon microalloying steel. Kawulokova et al. [24] employed the two cooling rates (0.0833 and 0.333 °C $s^{-1}$) to determine transformation temperature by DSC and dilatometry. DSC and dilatometry were also linked to detect the precipitation hardening of X5CrNiCuNb16-4 steel [25]. HT-LSCM and DSC are complementary techniques to characterize solid-state phase transformations in the $\gamma$-loop of the binary Fe–P system [26]. The inter-/intragranular ferrite transformation of 0.22 mass pct. C $Ti_2O_3$/TiN engineered steels was observed by HT-LSCM and measured by DSC [27]. Another combination of dilatometry and HT-LSCM was adopted to observe the intragranular ferrite transformation [28,29].

The purpose of the present study is to critically compare the accuracy of *in-situ* HT-LSCM and DSC with dilatometry in measuring solid-state phase transformations during austenite decomposition. Furthermore, it should be demonstrated that coupling DSC measurements and HT-LSCM observations can be used as a novel approach to establish CCT diagrams of advanced steel grades. In the first part of this work, dilatometry, DSC and HT-LSCM were applied to characterize the microstructure evolution in 0.4%C-1.8%Si-2.8%Mn-0.5%Al (in mass pct.) steel during constant cooling. The chemical composition represents a common alloying concept in the design of high-strength steels. Cooling rates (CR) were applied within the limited range for each piece of equipment used. Optical microscopy and hardness measurements of the samples were conducted *ex-situ*. The second part discusses the accuracy in determining ferrite, pearlite, bainite and martensite transformation temperatures. Finally, a CCT diagram for the steel grade investigated is proposed based on overall results by considering the applied heat treatment parameters.

## 2. Materials and methods

### 2.1. Sample preparation and chemical analysis

Samples of 50 g were produced in the high-frequency remelting (HFR) furnace Lifumat-Met-3.3-Vac from Linn High Therm GmbH (Eschenfelden, Germany). As the starting materials, technically pure iron cylinders (99.9 mass pct. Fe), metallic manganese flakes (99.89 mass pct. Mn), silicon lumps (Alfa Aesar, 99.9999 mass pct. Si, LOT# 61,600,760), high purity aluminum wire (Alfa Aesar, 99.999 mass pct. Al, LOT# 36,076) and a previously prepared Fe-4.4 mass pct. C alloy were used. The eutectic Fe–C alloy was melted in a 20 kg induction furnace using synthetic desulfurized graphite powder (Alfa

Aesar, LOT# BCBB5882). The melting was carried out in alumina crucibles under Ar 5.0 (purity 99.999%) over-pressure atmosphere. After 2 min of chemical homogenization by inductive bath movement, the melt was centrifugally cast into a copper mold [26,30]. The chemical analysis was determined using an optical emission spectrometer (OES), type Spectromax Version F (SPECTRO Analytical Instruments & Co.KG., Germany). The measured composition of the samples is listed as the average value in Table 1.

### 2.2. Differential scanning calorimetry (DSC)

Experiments were carried out in a DSC 404F1 Pegasus from NETZSCH Geraetebau GmbH (Selb, Germany) with a rhodium (Rh) furnace ($T_{max}$ = 1650 °C) and a platinum DSC sensor instrumented with type S thermocouples. During the measurement, the protective tube of the Rh furnace was flushed with Ar 5.0 (70 ml $min^{-1}$). A zirconium (Zr) getter was positioned below the DSC sensor to reduce the oxygen level at elevated temperatures (T > 350 °C) to a minimum. The DSC setup was calibrated by measuring the melting points and melting enthalpies of NETZSCH's standards of pure metals In, Bi, Al, Ag, Au, Ni and Co. $Al_2O_3$ crucibles (85 μl) with lids were used; the reference was an empty crucible. A detailed description of the current DSC setup can be found in references [30,31].

It is well known that the DSC signal is sensitive to the heat exchange during the phase transformation (ΔH) per scanning time Δt ($\Delta t = \Delta T \times SR^{-1}$, SR is the scanning rate in °C $s^{-1}$) [26]. It is a common practice to increase the scanning rate or change the sample mass to intensify the DSC signal for a phase transformation. M. Bernhard et al. [26] proposed that a sample mass of 250 mg (3.5 × 3.5 × 2.6 mm) is suitable in the current DSC setup to characterize solid-state transformations in steels accurately. This approach was followed in the recent study for evaluating the cooling curves defined in Section 2.6. For detailed information on the interpretation of DSC signals to determine phase transformation temperatures in alloys (e.g., the definition of onset and peak temperatures), the authors refer to the NIST Recommended Practice Guide [32]. The onset temperature represents the first deviation from the stable baseline and is associated with the beginning of a phase transformation. A peak temperature is defined as a local maximum of the DSC signal and generally represents the end of the respective phase transformation. However, it has to be noted that each phase transformation may show characteristic curves of the DSC charts, depending on the steel's alloying system.

### 2.3. High-temperature laser scanning confocal microscopy (HT-LSCM)

*In-situ* HT-LSCM has become an established tool to observe microstructural changes in steels up to the liquid state [26,30,33–35]. The experiments were carried out in a confocal laser scanning microscope VL2000DX manufactured by Lasertec (Yokohama, Japan) and a high-temperature furnace SVF17-SP from Yonekura (Yokohama, Japan). Small samples with 5 × 5 × 1.5 mm geometry were cut from the high-frequency remelted samples. The specimens were ground and polished. Within the HT-LSCM trials, the samples were put into alumina crucible and placed on the sample holder in the gold-coated, elliptical HT furnace. The furnace chamber was evacuated and flushed with Ar 5.0 to minimize the oxygen content. The temperature in the furnace was controlled using a type S thermocouple located at the bottom of the sample surface. A systematic referencing of the temperature was executed before every experimental campaign to determine the sample surface's temperature accurately. For this purpose, an external thermocouple was welded to the test-sample surface [36]. Throughout the experiment, a video was recorded with a maximum frame rate of 60 $s^{-1}$, enabling detailed studies of microstructure changes occurring post-experimentally due to the thermal etching effect [37].

**Table 1 – Chemical composition of the investigated steel grade.**

| C [mass pct.] | Si [mass pct.] | Mn [mass pct.] | Al [mass pct.] |
|---|---|---|---|
| 0.40 ± 0.004 | 1.79 ± 0.03 | 2.81 ± 0.04 | 0.51 |

### 2.4. Dilatometry

Dilatometry measurements at low cooling rates (Section 2.6) were performed by a dilatometer DIL Expedis SUPREME NanoEye from NETZSCH Geraetebau GmbH (Selb, Germany) with a corundum holder, push rod and S-type thermocouple. The inner space around the samples was evacuated and flushed with helium before each analysis. Temperature calibration (Ag, 99.999%) and calibration using standard expansion (corundum) were carried out before the experimental series. The samples were processed into cylinders with a diameter of 6.2 mm and a length of 9.7 mm. The mass of the cylinders was approximately 2250 mg. The dynamic high-purity atmosphere of He 6.0 (purity 99.9999%, flow rate 120 ml $min^{-1}$) was maintained during the analysis. The static force applied to the sample was 0.2 N.

Experiments with high cooling rates (Section 2.6) were performed on a dilatometer DIL 805A/D/T manufactured by TA Instruments (New Castle, USA). DIL 805 is a hardening quenching type dilatometer (A) with the possibility of deformation by pressure (D) and tension (T). Samples of 10 mm in length and 4 mm in diameter were inductively heated in a vacuum atmosphere to the austenitizing temperature and then continuously cooled at the defined cooling rate. The inductor consists of two coils, whereas the inner coil is used for gas quenching (N 5.0, purity ≥99.999%) and the outer coil is water-cooled. The measuring chamber consists of two parts, with the linear variable differential transformer (LVDT) monitoring the change in sample length on the one side and the sample mounted in the measuring system on the other. The measuring system for the quenching measuring head consists of three push rods and the thermocouple. The push rods are made of fused silica. The standard thermocouple Pt–Pt/Rh 10% (type S) was used to measure the temperature of the sample. The thermocouple was fixed to the sample by spot-welding technique. Before starting each experiment, a vacuum was created in the measuring chamber using nitrogen 5.0.

### 2.5. Microstructure characterization and hardness measurement

Subsequent to the DSC and dilatometry experiments, samples were cut off, embedded and prepared by mechanical polishing and etching with 4% nital to study the microstructure. Specimens of HT-LSCM were not considered for OM as the microstructural changes were observed *in-situ* on the surface. A Zeiss optical microscope (OM, Oberkochen, Germany) was used to observe the microstructure of all samples. An HV-1000A Vickers hardness tester measured the hardness of all samples (DSC, HT-LSCM and DIL) with a load of 50 g, and the average of five separate indentations was calculated as the final hardness.

### 2.6. Time-temperature profile and measurement of the initial austenite grain size (AGS)

In the first step, the $A_1$ and $A_3$ temperatures had to be determined to define the austenitizing temperature. The DSC method was used, applying a slow heating rate of 0.17 °C $s^{-1}$ (10 °C $min^{-1}$) and considering a small sample mass of 50 mg (1.5 × 1.5 × 2.1 mm) to reduce the thermal lag during scanning. The DSC charts of three independent measurements are plotted in Fig. 1 (note the signals are corrected to an arbitrary offset; the unit is given in μV). The onset for $A_1$ can be observed as an abrupt change in the DSC signal at 736.6 ± 0.3 °C. The minor peak below $A_1$ is the Curie temperature ($T_C$) given by 726.8 ± 1.6 °C. The $A_3$ temperature is detected at 858.5 ± 3 °C, represented as endset rather than forming a peak in the DSC signal.

Based on the measured value of $A_3$, the austenitizing temperature was set to 1000 °C. In all experiments, the samples were heated at 0.50 °C $s^{-1}$ to 1000 °C and kept stable for 5 min. Subsequently, the samples were cooled to room temperature with the CR defined explicitly for each piece of equipment.

- DSC and HT-LSCM: The current DSC setup is limited to a maximum CR of 0.50 °C $s^{-1}$. The minimum CR was considered with 0.05 °C $s^{-1}$ as slower cooling would significantly increase the experimental time and reduce the method's efficiency. Furthermore, only minor changes in the measured phase transformation temperatures are expected by further decreasing the CR. The HT-LSCM equipment enables cooling up to 20 °C $s^{-1}$. However, deviations from the linear CR must be accepted during fast cooling. Therefore, the highest cooling rate was defined as 10 °C $s^{-1}$. Prolonged cooling may result in surface oxidation of the sample. Based on pre-trials, the lowest CR of 0.20 °C $s^{-1}$ was reasonable to avoid any surface oxidation of the sample. By coupling the available DSC setup with the HT-LSCM method, a wide range of cooling cycles can be investigated (0.05–10 °C $s^{-1}$). To critically compare the obtained phase transformations by DSC and HT-LSCM, two similar cooling rates of 0.20 °C $s^{-1}$ and 0.50 °C $s^{-1}$ were applied in the CCT evaluation.
- DIL: The dilatometers were conserved as benchmark equipment to reconstruct the CCT diagram. The quenching dilatometer covered the high cooling rates (1–20 °C $s^{-1}$). The high-resolution dilatometer investigated the range of very slow cooling (0.05–0.50 °C $s^{-1}$).

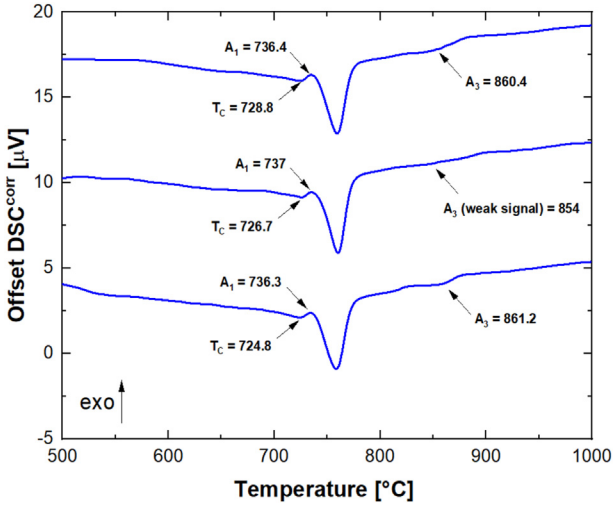


**Fig. 1 – DSC measurements of $A_1$ and $A_3$ temperature with a heating rate of 10 °C $min^{-1}$ (0.17 °C $s^{-1}$).**

During the isothermal holding step at 1000 °C, the austenite grains grow to minimize the system's free energy. The exact knowledge of the grain size at the start of cooling represents an essential parameter for evaluating the phase transformation temperatures and must be given for an accurately measured CCT. Large grains will delay the transformation started in diffusion-controlled mechanisms. Besides recording phase transformations, the HT-LSCM enables the determination of the grain size distribution, observed *in-situ* on the sample surface [36,38]. A high-resolution picture of the video was analyzed at the final stage of isothermal annealing at 1000 °C. As an example, the micrograph of the experiment with 0.5 °C $s^{-1}$ is shown in Fig. 2 (a). Due to the thermal etching effect, the grain boundaries are clearly visible. The statistical analysis is plotted in Fig. 2 (b). The log-normal distribution confirms normal grain growth (NGG) with a mean austenite grain size (AGS) of 60 μm. Identical values were obtained for all other experiments performed by HT-LSCM (0.2, 1, 5 and 10 °C $s^{-1}$) and were considered as representative for all *in-situ* trials by DSC, HT-LSCM and dilatometry.

The calculation of the CCT diagram in Fig. 3 (a) and (b) was performed using JMatPro software [39]. According to the HT-LSCM results, the initial AGS was set to 60 μm. The equilibrium temperatures $A_3$ and $A_1$ are predicted as 816.6 °C and 733.5 °C, respectively. $A_1$ is in reasonable agreement with the DSC measurements ($A_{1,DSC}$ = 736.6 °C), where more significant deviations are observed in the case of $A_3$ (ΔT ~ 40 °C). The bainite start temperature ($B_S$) at an infinite time is given by 457.8 °C and the martensite start temperature ($M_S$) is calculated to be 245 °C. At cooling rates lower than 0.25 °C $s^{-1}$, proeutectoid ferrite formation is expected, characterized by the temperature $F_S$. The transformation curve of ferrite is very close to the pearlite start temperature ($P_S$). Pearlite is stable up to a critical CR of about 5 °C $s^{-1}$. The calculation indicates that the alloying elements in the studied steel grade suppress the bainite formation and shift the start temperature ($B_S$) to longer

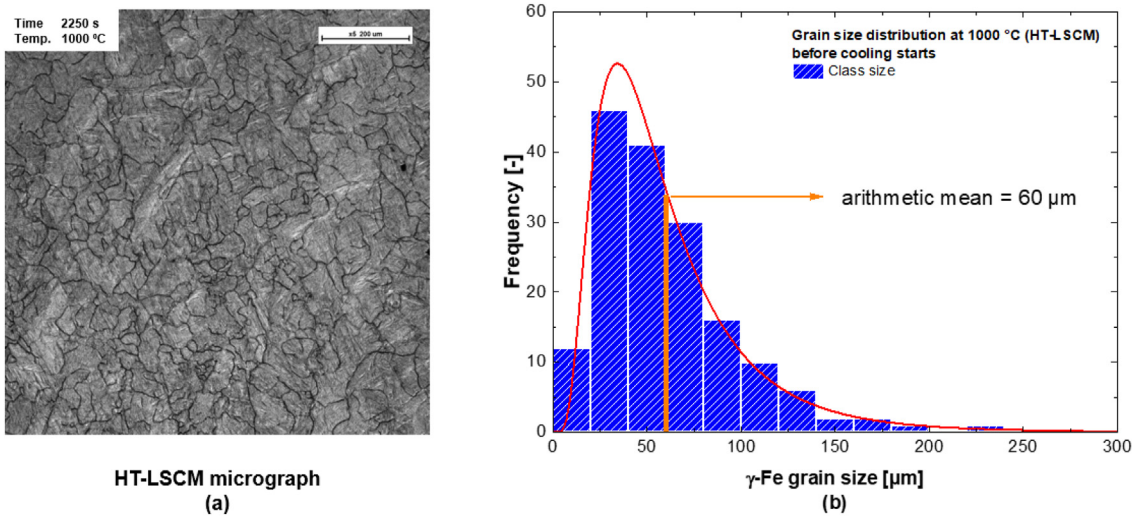


**Fig. 2 – Austenite grains at the final stage of isothermal annealing at 1000 °C (a) and analyzed AGS statistics (b).**

incubation times. The critical CR for a martensitic steel matrix is 5 °C $s^{-1}$.

## 3. Results and discussion

In the first section, the results of each *in-situ* technique are analyzed individually, supported by the OM results and hardness measurements. In the second part, the CCT is reconstructed and the potential and limitations of the experimental methods used are discussed critically.

### 3.1. *Phase transformation temperatures and microstructure analysis*

#### 3.1.1. *DSC analysis*

Fig. 4 (a) graphically summarizes all DSC signals obtained during cooling at 0.05–0.50 °C $s^{-1}$. Note that the DSC charts were corrected by an arbitrary offset; the unit is µV. The first onset in the signal may be assigned to the pearlite start temperature ($P_S$), with a significant heat exchange during slow cooling (0.05–0.25 °C $s^{-1}$). The intensity of the DSC signal decreases with increasing cooling rate due to a less forming fraction of pearlite. As expected, $P_S$ is shifted to lower values at higher CR. No pearlite was identified at the CR of 0.35 and 0.50 °C $s^{-1}$.

Austenite transformation to martensite is detected in the low-temperature range (T < 300 °C). Martensite forms already at a prolonged cooling rate of 0.10 °C $s^{-1}$. The phase fraction of martensite, and as a consequence, the DSC signal's intensity, continuously increases if the CR is increased. The $M_S$ seems to be slightly dependent on the CR. $M_S$ first increases and becomes constant at CR $\geq$ 0.25 °C $s^{-1}$ with the average value of $M_S$ = 270 °C. $M_S$ is strongly affected by preliminary phase transformations. Due to the larger consumption of austenite to form pearlite at a CR of 0.10 °C $s^{-1}$, less austenite is available

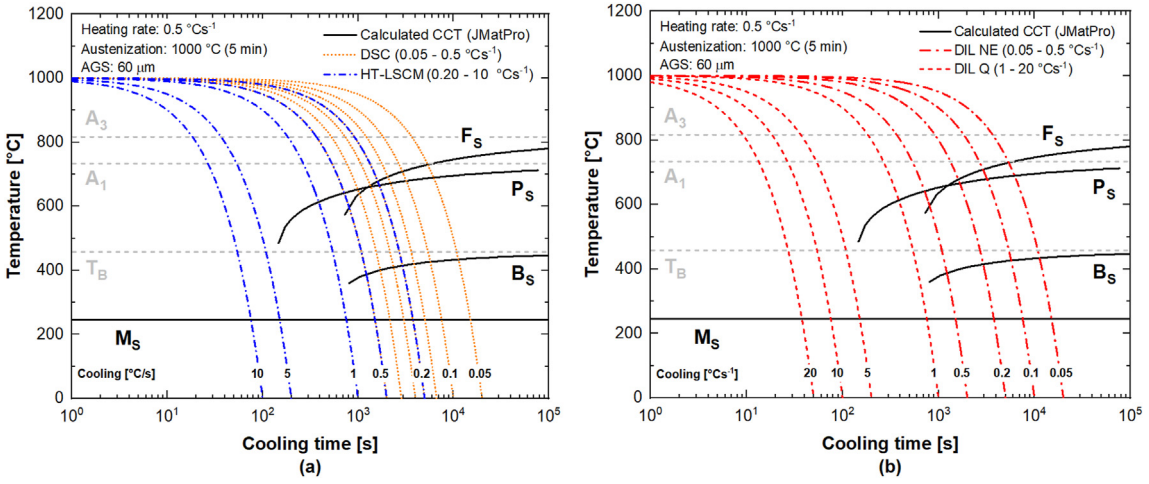


**Fig. 3 – Cooling rates defined in HT-LSCM and DSC trials (a) and DIL (b) along with the CCT calculated using JMatPro software [39]. DIL NE … DIL Expedis SUPREME NanoEye. DIL Q … DIL 805A/D/T.**

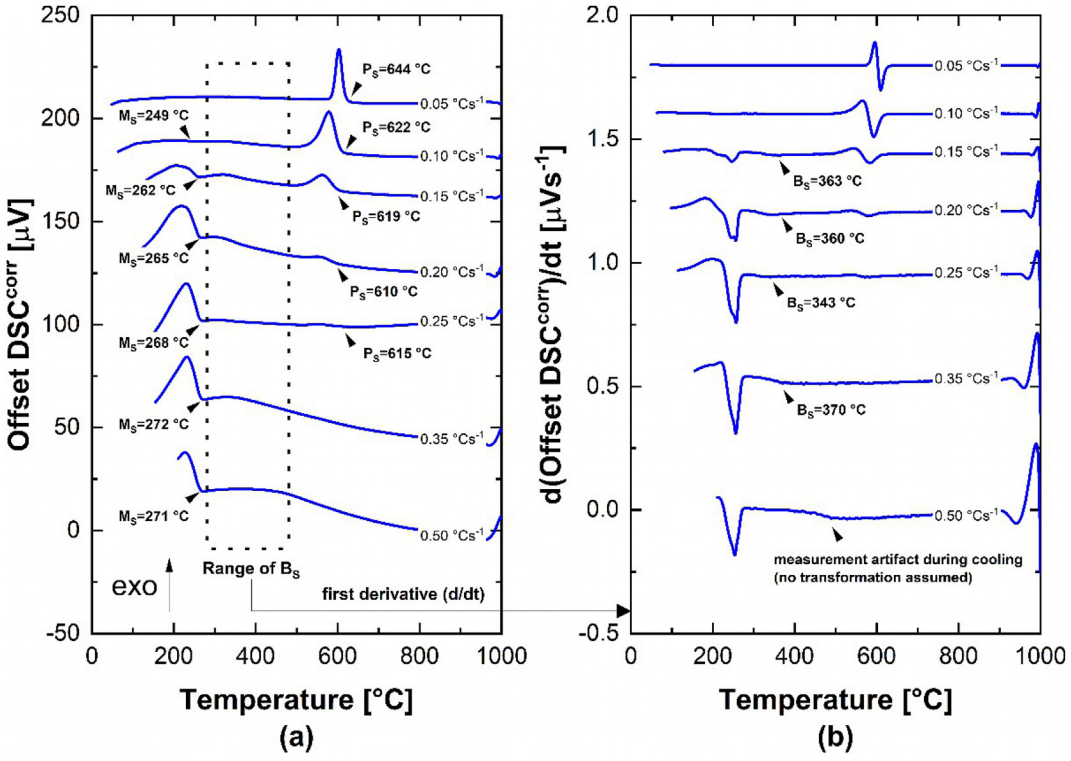


**Fig. 4 – Offset of DSC signals during cooling with 0.05–0.50 °C $s^{-1}$, corrected to the baseline of 0 µV (a) and first derivative by time for obtaining the $B_S$ temperature (b).**

for martensite, resulting in a lower $M_S$ of 249 °C. The decreased intensity of the DSC signal of $P_S$ with higher CR indicates less decomposition of austenite into pearlite. Hence, more untransformed austenite is available for the bainite and martensite transformations. At the same time, the DSC signal of bainite transformation is very weak. Thus, martensite transformation happens at a higher temperature, indicated by the increase of $M_S$ at the CR of 0.15–0.25 °C $s^{-1}$. At 0.50 °C $s^{-1}$, martensite is the primary phase, and $M_S$ becomes constant.

Between 500 and 300 °C, a change in the DSC signal is evident in Fig. 4 (a). Depending on the alloying concept of the steel grade, the bainite formation usually starts in this intermediate temperature range. However, an accurate prediction of the $B_S$ temperature is challenging in the original charts. The first derivative by time is plotted in Fig. 4 (b), representing the transformation rate in µV $s^{-1}$. From Fig. 4 (b), the $B_S$ temperature becomes visible as a deviation from the actual signal trend line at CR of 0.15–0.35 °C $s^{-1}$. The enlarged section of the bainite formation is plotted in Fig. 5. Bainite growth starts at a temperature close to that of martensite. The critical cooling rate of bainite formation is obtained by 0.50 °C $s^{-1}$, above which no bainite forms at a slower CR. However, as expected from the CCT calculations in Fig. 3, a clear dependence on the CR is not established.

Fig. 6 shows the micrographs of all DSC samples analyzed by OM (4% nital etchant). The obtained microstructure constituents and corresponding hardness values are summarized along with the DSC results in Table 2. At CR of 0.05–0.20 °C $s^{-1}$, small fractions of pro-eutectoid ferrite are observed along the prior austenite grains. The ferrite formation could not be obtained in the DSC signal, as the ferrite fraction formed was too low and the resulting heat change was below the resolution limit of the DSC setup. Furthermore, the CCT calculations in Fig. 3 indicate that ferrite starts to grow nearly simultaneously along with pearlite, which may lead to less clear phase separation in the DSC chart.

Pearlite is the dominant microstructure constituent in samples cooled at 0.05 and 0.10 °C $s^{-1}$; the amount continuously decreases with a higher CR. At 0.35 °C $s^{-1}$ and 0.50 °C $s^{-1}$,

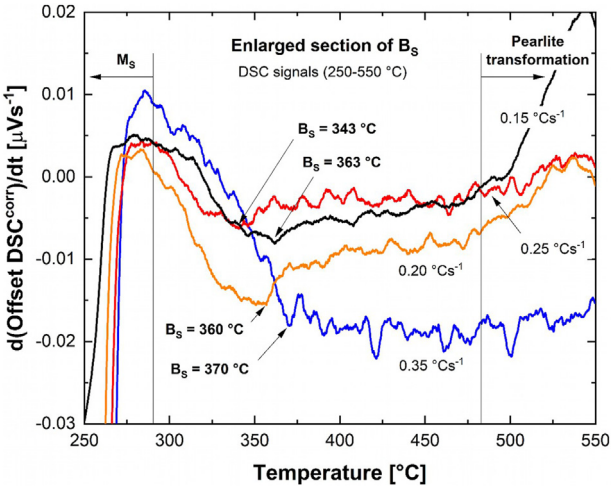


**Fig. 5 – DSC transformation rate in the enlarged section of the bainite formation for cooling rates of 0.15–0.35 °C $s^{-1}$.**

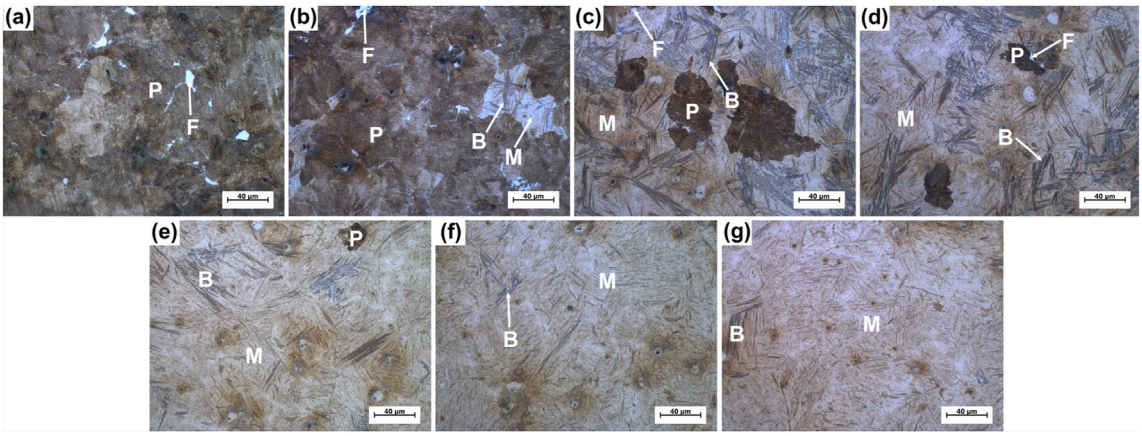


**Fig. 6 – Optical microstructure of DSC samples at different cooling rates. 0.05 °C $s^{-1}$ (a), 0.10 °C $s^{-1}$ (b), 0.15 °C $s^{-1}$ (c), 0.20 °C $s^{-1}$ (d), 0.25 °C $s^{-1}$ (e), 0.35 °C $s^{-1}$ (f) and 0.50 °C $s^{-1}$ (g). (F: ferrite; P: pearlite; B: bainite; M: martensite).**

no pearlite can be found in the micrographs, which is in excellent agreement with the DSC analysis. The highest fractions of bainite can be observed in Fig. 6 (c) and (d), corresponding to cooling rates of 0.15 and 0.20 °C $s^{-1}$. In this case, the most significant change in the DSC signals was also detected. However, the amount of bainite in Fig. 6 (b) (CR = 0.10 °C $s^{-1}$) was too low to observe accurately in the DSC measurements. Martensite is observed from 0.10 to 0.50 °C $s^{-1}$ in Fig. 6 (b)–(g). Based on the DSC analysis and the micrographs, the critical CR, above which only martensite is obtained, is higher than 0.50 °C $s^{-1}$.

### 3.1.2. *HT-LSCM observations*

Fig. 7 shows the occurrence of phase transformations during different cooling. White ellipses point out the positions where the phase transformation happens. The transformation type can be determined based on the characteristics of phase transformation products in conjunction with the temperature. Pearlite nucleated at prior austenite grain boundaries, growing into the austenite grains. The morphology of pearlite was an irregular shape. Bainite and martensite nucleated at the grain or phase boundaries and developed in a lath morphology. The main difference between bainite and martensite is the growth rate. Lath bainite occurred gradually, while lath martensite happened instantaneously and widely. The formation of ferrite could not be observed at any cooling rate. However, it must be noted that the range of adjustable magnification is limited during the investigation of CCT by HT-LSCM. A high magnification, which would be required to detect minor phase fractions forming from a single austenite grain, shows the disadvantage that the observation may not represent the whole sample surface.

At a higher cooling rate, the sample does not stay long in the higher temperature region, indicating that a larger driving force is required for pearlite transformation. Hence, $P_S$ gradually decreases from 0.20 to 1 °C $s^{-1}$ from 604 °C to 553 °C. The critical cooling rate at which pearlite does not form anymore is 5 °C $s^{-1}$. $B_S$ first increases and then decreases, while $M_S$ changes differently when increasing the cooling rate from 0.2 to 10 °C $s^{-1}$. Lower $P_S$ means lower consumption of austenite. In this case, the remaining austenite is easily transformed to bainite, showing an increase in $B_S$ within 0.20–1 °C $s^{-1}$. As the bainite transformation is accompanied by carbon diffusion, less austenite with high carbon concentration is retained and $M_S$ decreases. When increasing the cooling rate, a more considerable undercooling degree for bainite transformation is needed, resulting in a decrease in $B_S$. If austenite decomposes in less bainite fraction, more untransformed austenite is available for the martensite transformation; consequently, $M_S$ increases. The determined phase transformations and the observed microstructure constitution are listed in Table 3 along with the measured hardness.

### 3.1.3. *Dilatometry*

Fig. 8 depicts the measured dilation curves for several cooling rates, represented versus temperature and given by an

**Table 2 – DSC results of transformation temperatures compared with microstructure constituents obtained in the optical microscope.**

| Cooling rate [°C$s^{-1}$] | Ps [°C] | Bs [°C] | Ms [°C] | Phase (*in-situ*) | Phase (OM) | Hardness [$HV_{0.05}$] |
|---|---|---|---|---|---|---|
| 0.05 | 644 | – | – | P | P + F | 316 ± 4 |
| 0.10 | 622 | – | 249 | P + M | P + F + B + M | 325 ± 17 |
| 0.15 | 619 | 363 | 262 | P + B + M | P + F + B + M | 494 ± 33 |
| 0.20 | 610 | 360 | 265 | P + B + M | P + F + B + M | 512 ± 21 |
| 0.25 | 615 | 343 | 268 | P + B + M | P + B + M | 608 ± 16 |
| 0.35 | – | 370 | 272 | B + M | B + M | 612 ± 18 |
| 0.50 | – | – | 271 | M | B + M | 614 ± 16 |

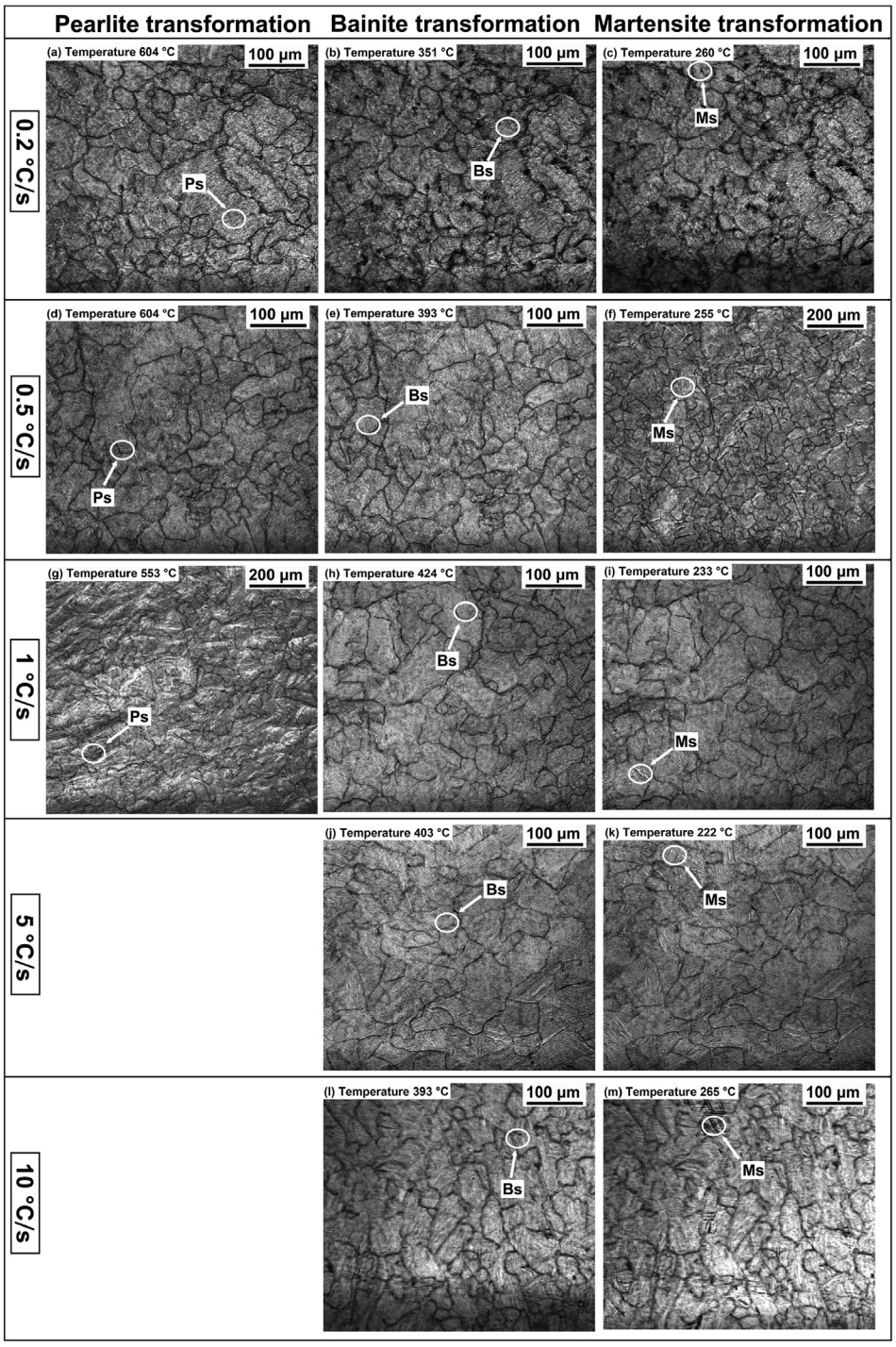


**Fig. 7 – The occurrence of phase transformations at different CRs and their corresponding optical microstructures: 0.2 °C $s^{-1}$ (a)–(c), 0.5 °C $s^{-1}$ (d)–(f), 1 °C $s^{-1}$ (g)–(i), 5 °C $s^{-1}$ (j)–(k) and 10 °C $s^{-1}$ (l)–(m).**

arbitrary offset. Depending on the cooling rate, the shape of the curve and the transformation temperatures vary. $P_S$ is lowered as the cooling rate increases, whereas the $M_S$ points of samples at higher cooling rates seem stable within 271–282 °C; see Fig. 8 (b). The transformed fraction curve exhibits several slope changes in the particular cases of 0.20 °C $s^{-1}$ and 0.50 °C $s^{-1}$ as well as 0.10 °C $s^{-1}$ and 1 °C $s^{-1}$. For other cooling rates, and even if the optical micrographs show that the microstructures are composed of a mixture of different phases, only one phase transformation was recorded by expansion. It should be mentioned that the critical cooling rate for pure pearlite transformation is 0.05 °C $s^{-1}$, above

**Table 3 – HT-LSCM results of transformation temperatures compared with microstructure constituents obtained in the optical microscope.**

| Cooling rate [ °Cs$^{-1}$] | Ps [°C] | Bs [°C] | Ms [°C] | Phase (*in-situ*) | Hardness [$HV_{0.05}$] |
|---|---|---|---|---|---|
| 0.2 | 604 | 351 | 260 | P + B + M | 510 ± 26 |
| 0.5 | 604 | 393 | 255 | P + B + M | 603 ± 24 |
| 1 | 553 | 424 | 233 | P + B + M | 610 ± 22 |
| 5 | – | 403 | 222 | B + M | 598 ± 21 |
| 10 | – | 393 | 265 | B + M | 600 ± 13 |

which other phase transformations happened during cooling. The required cooling rate for pure martensite transformation is 5 °C s$^{-1}$.

Additional information can be extracted if the slope of the dilatation is given by the first derivative by time (dD/dt). The analysis to recognize the transformation types based on this approach is demonstrated in Fig. 9, showing the transformation rates as a function of the temperature. For the 0.20 and 0.50 °C s$^{-1}$ cooling rates, three different peaks correspond to the formation of the pearlite, bainite and martensite mixture. At cooling rates of 1 °C s$^{-1}$, the transformation rate curve has a sharp and narrow peak related to the formation of pearlite. Similar to the DSC analysis, the onset of the peak is considered the start of the transformation.

For the dilation curves to be interpreted, a careful and systematic analysis of resulting data in conjunction with optical micrographs in Fig. 10 was done (4% nital etchant). Though dilatation curves do not recognize ferrite transformation, it is observed by optical micrographs at the CR below 0.05 °C s$^{-1}$, as pointed out by arrows in Fig. 10 (a)–(d). The proportion of ferrite and pearlite fractions decreases with an increasing CR and disappears when the CR is larger than 0.5 °C s$^{-1}$. The martensite phase starts at 0.1 °C s$^{-1}$ and increases when the CR is raised to 0.5 °C s$^{-1}$. Martensite consequently becomes the main phase in the microstructure of samples at the CR of 1–20 °C s$^{-1}$. The bainite structure begins to form at the CR of 0.2 °C s$^{-1}$ and disappears when the CR is above 0.5 °C s$^{-1}$. The corresponding hardness response of samples at different CRs is listed in Table 4.

### 3.2. *CCT diagrams: critical evaluation of techniques used* in-situ *and future perspectives*

Fig. 11 (a) and Fig. 11 (b) show the experimental CCT diagrams determined by HT-LSCM and DSC and dilatometry, respectively. Calculations performed with JMatPro software [39] are plotted for comparison. Though pro-eutectoid ferrite was identified in the OM analysis of a sample cooled at 0.05–0.20 °C s$^{-1}$, its formation could not be measured by any *in-situ* technique. The ferrite transformation curve is close to the pearlite transformation curve, as presented by the dashed lines calculated by JMatPro software. Hence, it is reasonable to speculate that the ferrite transformation happens first and then the pearlite transformation occurs quickly. The ferrite and pearlite transformations may overlap, which could not be distinguished from dilation curves. In addition, it can be concluded that all methods show a limited resolution in this case. The $P_S$ excellently agrees between HT-LSCM/DSC and DIL. The HT-LSCM performs better than the DSC in measuring $P_S$ at CR > 0.35 °C s$^{-1}$. DIL enables the determination of $P_S$ up to a CR of 1 °C s$^{-1}$, as can be seen in Fig. 11 (b). The data sets obtained are in good accordance with the calculations. In

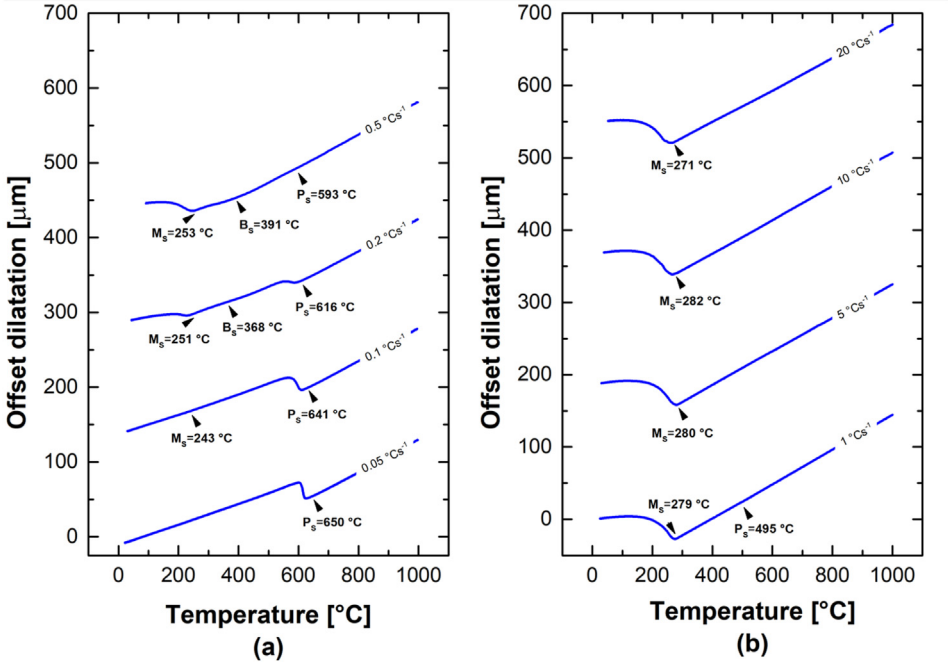


**Fig. 8 – Dilatation curves of high-resolution dilatometer at CR of 0.05–0.50 °C s$^{-1}$ (a) and CR of 1–20 °C s$^{-1}$ (b).**

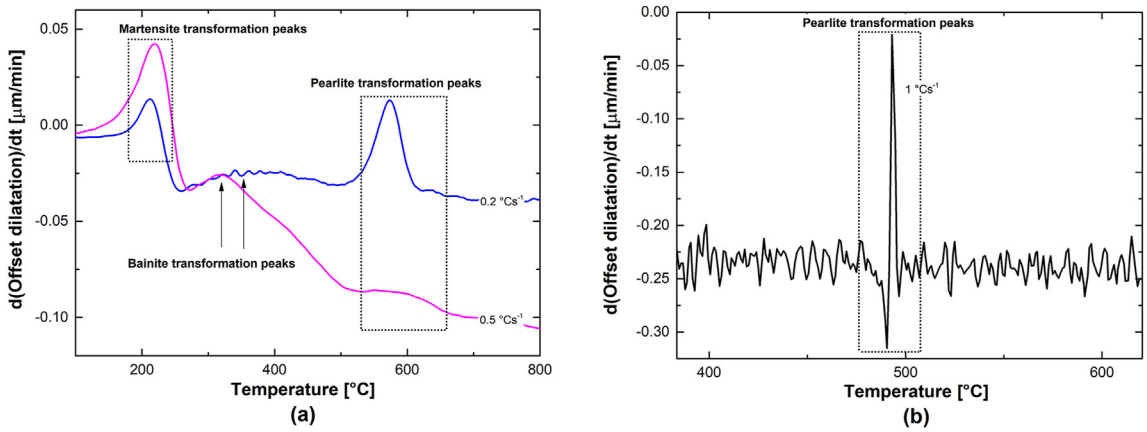


**Fig. 9 – DIL transformation rate for 0.20 and 0.50 °C $s^{-1}$ (a) and enlarged section of pearlite formation at the cooling of 1 °C $s^{-1}$ (b).**

general, slightly lower values of $P_S$ were measured. HT-LSCM provides a valuable option to observe $B_S$ even at minor forming fractions of bainite and higher CR. Concerning the DSC, phase transformations are accompanied by exothermic peaks, and the integrated intensity represents the transformation fraction semi-quantitatively. It should be mentioned that the determination of bainite starting temperature may cause a specific extent deviation from the real one due to the relatively flat exothermic peak. However, minor peaks of bainite transformation are still recorded to prove the occurrence of bainite transformation during the cooling process. At cooling rates of 0.20 and 0.50 °C $s^{-1}$, the DIL equipment used shows a deviation from linear expansion at $B_S$ = 368 °C and $B_S$ = 391 °C, respectively. The increase in $B_S$ with CR agrees with the HT-LSCM/DSC results, which are difficult to predict by empirical-mathematical models. Usually, the calculated phase transformation curves are represented by the classic nose-shaped nucleation boundaries; see calculated $F_S$, $P_S$ and $B_S$ in Fig. 11 (a) and **(b)**. $M_S$ is accompanied by a significant change in the DSC and DIL signals and is visible in the HT-LSCM observations. $M_S$ temperature is well predicted in the calculations.

The hardness response, graphically represented in Fig. 12, depends on the microstructure. From DSC samples, the hardness remains stable when the CR is below 0.10 °C $s^{-1}$, then increases with the CR of 0.10–0.25 °C $s^{-1}$, and finally becomes constant again when the CR is above 0.25 °C $s^{-1}$. The change tendency of hardness is in good agreement with the microstructural evolution in Fig. 6. A similar hardness trend is obtained in the HT-LSCM and dilatometry samples, along with the corresponding micrographs in Figs. 7 and 10. The hardness rises from 510 HV at 0.2 °C $s^{-1}$ to 610 H HV at 1 °C $s^{-1}$, which can be assigned to the steady increase of hard phases like martensite and bainite in the microstructure. At the CR of 1–20 °C $s^{-1}$, the microstructure shows a stable hardness response within 607–614 HV.

Based on the results, DSC, HT-LSCM and DIL measure the phase transformation temperature with sufficient accuracy. The phase transformation temperatures at the same cooling rate detected by different methods correspond well. Coupling DSC and HT-LSCM is, therefore, a powerful approach to accurately establish a CCT diagram in future research. The present study's complementary use of DSC and HT-LSCM shows identical resolution limits for measuring $P_S$ and $M_S$ as the well-

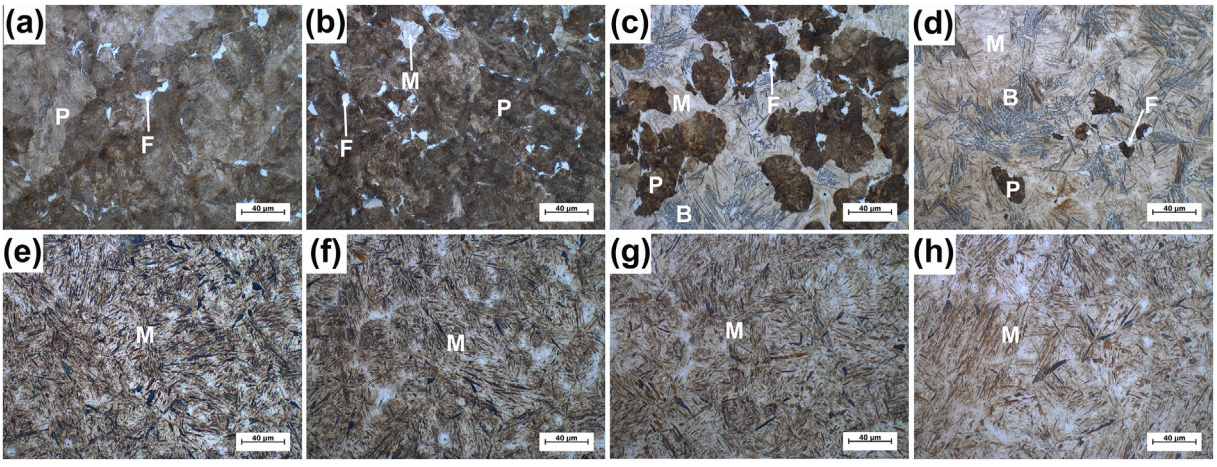


**Fig. 10 – Optical microstructure of dilatometry samples at different cooling rates: 0.05 °C $s^{-1}$ (a), 0.10 °C $s^{-1}$ (b), 0.20 °C $s^{-1}$ (c), 0.50 °C $s^{-1}$ (d), 1.0 °C $s^{-1}$ (e), 5.0 °C $s^{-1}$ (f), 10.0 °C $s^{-1}$ (g) and 20.0 °C $s^{-1}$ (h). (F: ferrite; P: pearlite; B: bainite; M: martensite).**

**Table 4 – Dilatometer results of transformation temperatures compared with microstructure constituents obtained in the optical microscope.**

| Cooling rate [°Cs$^{-1}$] | Technique | Ps [°C] | Bs [°C] | Ms [°C] | Phase (*in-situ*) | Phase (OM) | Hardness [$HV_{0.05}$] |
|---|---|---|---|---|---|---|---|
| 0.05 | DIL NE[a] | 650 | – | – | P | F + P | 306 ± 11 |
| 0.1 | DIL NE | 641 | – | 243 | P + M | F + P + M | 334 ± 23 |
| 0.2 | DIL NE | 616 | 368 | 251 | P + B + M | F + P + B + M | 504 ± 29 |
| 0.5 | DIL NE | 593 | 391 | 253 | P + B + M | F + P + B + M | 608 ± 26 |
| 1 | DIL Q[b] | 495 | – | 279 | P + M | M | 610 ± 24 |
| 5 | DIL Q | – | – | 280 | M | M | 607 ± 22 |
| 10 | DIL Q | – | – | 282 | M | M | 614 ± 26 |
| 20 | DIL Q | – | – | 271 | M | M | 612 ± 23 |

[a] DIL Expedis SUPREME NanoEye.
[b] DIL 805A/D/T.

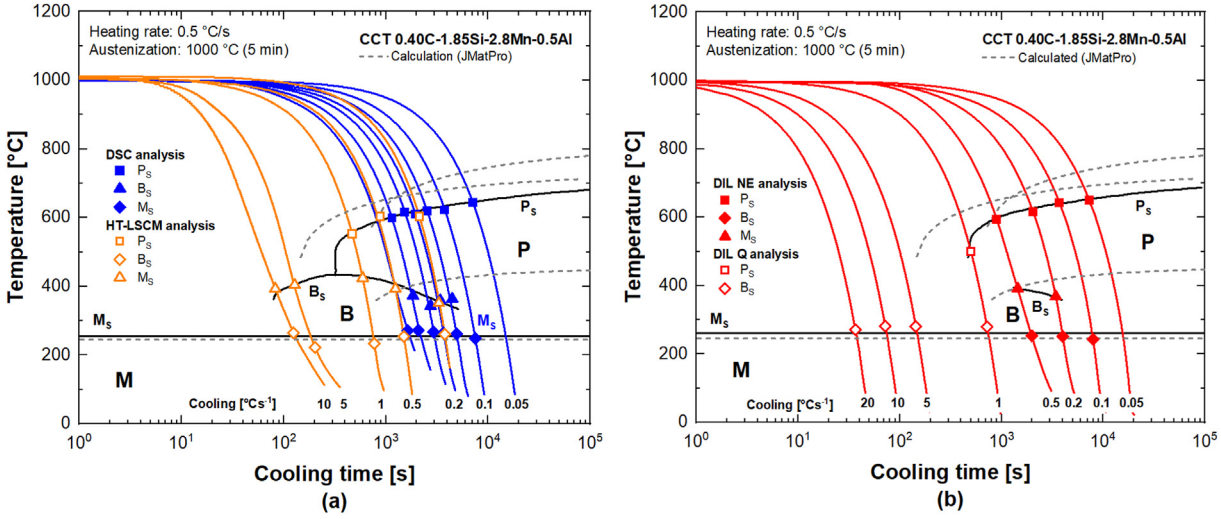


**Fig. 11 – CCT diagram for the tested steel grade reconstructed by DSC and HT-LSCM (a) and dilatometry (b) Full lines indicate the experimental transformation curves of $P_S$, $B_S$ and $M_S$. DIL NE … DIL Expedis SUPREME NanoEye. DIL Q … DIL 805A/D/T.**

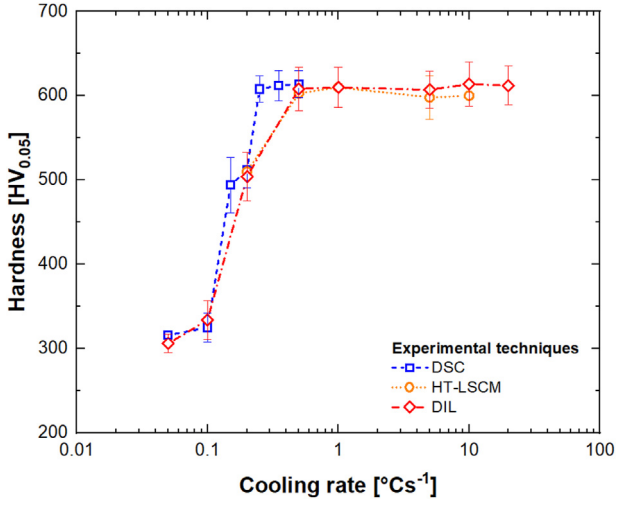


**Fig. 12 – Hardness response of DSC, HT-LSCM and DIL depending on the applied cooling rate.**

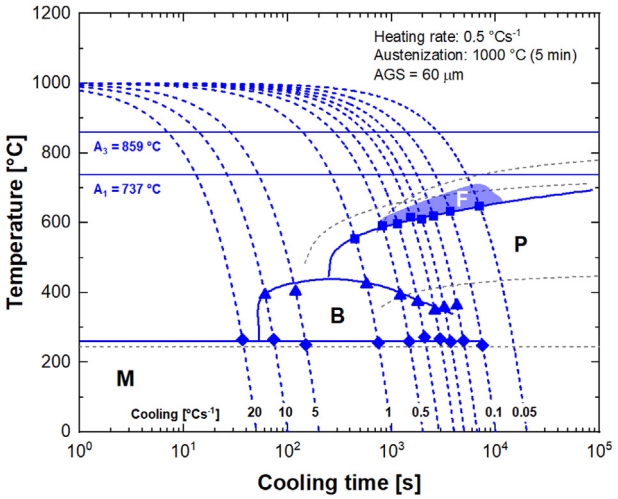


**Fig. 13 – CCT diagram observed by combining results of in-situ techniques (DSC, HT-LSCM and DIL) with OM analysis. Dashes indicate the phase transformation temperatures calculated with JMatPro [39], solid lines were observed experimentally in this study.**

**Table 5 – Summary of obtained phase transformations using DSC, HT-LSCM and DIL, given as the average value. OM results are also listed.**

| CR [°Cs$^{-1}$] | Technique | Ps [°C] | Bs [°C] | Ms [°C] | Phase (+OM) | Hardness [$HV_{0.05}$] |
|---|---|---|---|---|---|---|
| 0.05 | DSC + DIL | 647 | – | – | P + B + M (+F) | 315 ± 4 |
| 0.10 | DSC + DIL | 641 | – | 246 | P + B + M (+F) | 328 ± 14 |
| 0.15 | DSC | 619 | 363 | 262 | P + B + M (+F) | 494 ± 33 |
| 0.20 | DSC + DIL + HT-LSCM | 610 | 360 | 259 | P + B + M (+F) | 509 ± 14 |
| 0.25 | DSC | 615 | 343 | 268 | P + B + M | 608 ± 16 |
| 0.35 | DSC | – | 370 | 272 | P + B + M | 612 ± 18 |
| 0.50 | DSC + DIL + HT-LSCM | 599 | 392 | 260 | P + B + M (+F) | 610 ± 12 |
| 1 | HT-LSCM + DIL | 524 | 424 | 256 | P + B + M | 610 ± 16 |
| 5 | HT-LSCM + DIL | – | 403 | 251 | B + M | 602 ± 15 |
| 10 | HT-LSCM + DIL | – | 393 | 274 | B + M | 603 ± 12 |
| 20 | DIL | – | – | 271 | M | 612 ± 23 |

established dilatometry method. Due to the minor fraction of ferrite formed during cooling and possible overlap with $P_S$, it was impossible to identify the ferrite starting temperature in the *in-situ* measurements. It was not easy to monitor the bainite transformation in the intermediate temperature range directly from the dilatation curve. Supportively, the bainite transformation is revealed by the transformation rate versus temperature curves, as shown in Fig. 9. HT-LSCM provides the most detailed information on $B_S$ for the steel grade investigated. HT-LSCM directly and dynamically observes all phase transformations during the cooling process.

From the perspective of efficiency and convenient experimental procedure, the DSC technique is a powerful method to measure phase transformations. However, conducting experiments with higher cooling rates requires specific setups. Dilatometry is extensively employed in literature to determine transformation temperature due to its wide application range. Similar to DSC, the sensitivity of dilatometry depends on the change in the measured physical properties (heat change or thermal expansion), which is limited if only a small transformation amount is formed. Though HT-LSCM records most of the expected phase transformations, this technique is not popular yet to establish CCT diagrams due to strict experimental conditions concerning possible surface oxidation and temperature calibration.

Finally, a comprehensive CCT diagram of the 0.40%C-1.80%Si-2.80%Mn-0.50%Al steel grade is plotted in Fig. 13, considering the heating rate of 0.50 °C s$^{-1}$ to the austenitizing temperature of 1000 °C and the initial AGS of 60 μm. Additionally, the results of optical metallography indicate the presence of ferrite. The average temperatures are listed in Table 5. The critical CR to obtain bainite and martensite phases is 5 °C s$^{-1}$, and the CR for pure martensite is 20 °C s$^{-1}$.

## 4. Conclusion

The present study aimed to critically compare differential scanning calorimetry (DSC), high-temperature laser scanning confocal microscopy (HT-LSCM) and dilatometry (DIL) methods for establishing CCT diagrams of steel. For this purpose, a common 0.40%C-1.80%Si-2.80%Mn-0.50%Al alloying concept for high-strength steels was selected. Classic optical microscopy and hardness measurements were performed to evaluate the results. In measuring the phase transformation start temperatures of pearlite ($P_S$), bainite ($B_S$) and martensite ($M_S$), similar accuracy was obtained between coupling DSC results and HT-LSCM observation with the well-established DIL analysis. HT-LSCM provided the most detailed information on $B_S$ for the steel grade investigated. Finally, a comprehensive CCT diagram was plotted based on the overall DSC, dilatometry and HT-LSCM results. The critical cooling rate to obtain bainite and martensite phases is 5 °C s$^{-1}$, and the required cooling rate to get pure martensite is 20 °C s$^{-1}$. The present study shows, that coupling of HT-LSCM and DSC is a powerful method to plot CCT diagrams for future research on advanced steel grades.

## Data availability

The raw/processed data required to reproduce these findings cannot be shared at this time due to technical or time limitations.

## Author contributions

**Man Liu** and **Michael Bernhard:** Conceptualization and methodology, characterization, visualization, writing - original draft. **Monika Kawuloková:** Characterization, writing - review and editing. **Josef Walek:** Characterization, writing - review and editing. **Maximilian Kern:** Characterization, writing - review and editing. **Simona Zlá**: Characterization, writing - review and editing. **Peter Presoly:** Project administration, writing - review and editing. **Bedrich Smetana**: Writing - review and editing. **Marketa Tkadlečková:** Writing - review and editing. **Guang Xu:** Writing - review and editing. **Youn-Bae Kang:** Project administration, writing - review and editing. **Christian Bernhard:** Project administration, writing - review and editing.

## Declaration of competing interest

The authors declare that they have no known competing financial interests or personal relationships that could have appeared to influence the work reported in this paper.

## Acknowledgments

Michael Bernhard, Maximilian Kern, Peter Presoly and Christian Bernhard gratefully acknowledge the financial support under the scope of the COMET program within the K2 Center "Integrated Computational Material. Process and Product Engineering (IC-MPPE)" (Project No 859480). This program is supported by the Austrian Federal Ministries for Climate Action, Environment, Energy, Mobility, Innovation, and Technology (BMK) and for Digital and Economic Affairs (BMDW), represented by the Austrian research funding association (FFG), and the federal states of Styria, Upper Austria and Tyrol. This research was also partially supported by the Brain Pool program funded by the Ministry of Science and ICT through the National Research Foundation of Korea (NRF-2022H1D3A2A01081708). Man Liu gratefully acknowledges the support from the State Scholarship Fund of the China Scholarship Council. Monika Kawuloková, Josef Walek, Simona Zlá, Bedrich Smetana and Marketa Tkadlečková gratefully acknowledge the financial support for the project No. CZ.02.1.01/0.0/0.0/17_049/0008399 from the European Union and Czech Republic financial funds provided by the Operational Programme Research, Development and Education, Call 02_17_049 Long-Term Intersectoral Cooperation for ITI, Managing Authority: Czech Republic-Ministry of Education and student grant project SP2023/034 and SP2023/022.

## REFERENCES

[1] Trzaska J, Dobrzanski LA. Modelling of CCT diagrams for engineering and constructional steels. J Mater Process Technol 2007;192–193:504–10.
[2] Zheng SH, Wu QS, Huang QY, Liu SJ, Han YY. Influence of different cooling rates on the microstructure of the HAZ and welding CCT diagram of CLAM steel. Fusion Eng Des 2011;86:2616–9.
[3] Zhao JC, Notis MR. Continuous cooling transformation kinetics versus isothermal transformation kinetics of steels: a phenomenological rationalization of experimental observations. Mater Sci Eng R Rep 1995;15:135–207.
[4] Ali M, Nyo T, Kaijalainen A, Javaheri V, Tervo H, Hannula J, Somani M, Komi J. Incompatible effects of B and B + Nb additions and inclusions' characteristics on the microstructures and mechanical properties of low-carbon steels. Mater Sci Eng, A 2021;819:141453.
[5] Krbata M, Krizan D, Eckert M, Kaar S, Dubec A, Ciger R. Austenite decomposition of a lean medium Mn steel suitable for quenching and partitioning process: comparison of CCT and DCCT diagram and their microstructural changes. Materials 2022;15:1753.
[6] Lan LY, Chang ZY, Fan PH. Exploring the difference in bainite transformation with varying the prior austenite grain size in low carbon steel. Metals 2018;8:988.
[7] Ghosh SK, Chattopadhyay PP, Haldar A, Ganguly S, Datta S. Design of the directly air-cooled pearlite-free multiphase steel from CCT diagrams developed using ANN and dilatometric methods. ISIJ Int 2008;48:649–57.
[8] Miettinen J, Koskenniska S, Somani M, Louhenkilpi S, Pohjonen A, Larkiola J, Kömi J. Optimization of the CCT curves for steels containing Al, Cu and B. Metall Mater Trans B 2019;50:2853–66.
[9] Pohjonen A, Somani M, Porter D. Modelling of austenite transformation along arbitrary cooling paths. Comput Mater Sci 2018;150:244–51.
[10] Kirkaldy JS, Venugopolan D. Phase transformations in ferrous alloys. Warrendale: AIME; 1984. p. 125–32.
[11] Ali M, Porter D, Kömi J, Eissa M, Mattar T. Effect of cooling rate and composition on microstructure and mechanical properties of ultrahigh-strength steels. J Iron Steel Res Int 2019;26:1350–65.
[12] Mein A, Fourlaris G, Crowther D, Evans P. Influence of aluminum additions upon CCT diagrams for hot rolled TRIP assisted dual phase steel. Mater Sci Technol 2012;28(5):627–33.
[13] Wang ZH, Hui WJ, Chen Z, Zhang YJ, Zhao XL. Effect of vanadium on microstructure and mechanical properties of bainitic forging steel. Mater Sci Eng, A 2020;771:138653.
[14] Siwecki T, Eliasson J, Lagneborg R, Hutchinson B. Vanadium microalloyed bainitic hot strip steels. ISIJ Int 2010;50:760–7.
[15] Gomez M, Rancel L, Escudero E, Medina SF. Phase Transformation under continuous cooling conditions in medium carbon microalloyed steels. J Mater Sci Technol 2014;30(5):511–6.
[16] Kim KS, Du LX, Gao CR. Influence of vanadium content on bainitic transformation of a low-carbon boron steel during continuous cooling. Acta Metall Sin 2015;28:692–8.
[17] Huda N, Midawi A, Gianetto JA, Gerlich AP. Continuous cooling transformation behaviour and toughness of heat-affected zones in an X80 line pipe steel. J Mater Res Technol 2021;12:613–28.
[18] Halmešová K, Procházka R, Koukolíková M, Džugan J, Konopík P, Bucki T. Extended continuous cooling transformation (CCT) diagrams determination for additive manufacturing deposited steels. Materials 2022;15:3076.
[19] Kumar JVT, Sudha J, Padmanabhan KA, Frolova AV, Stolyarov VV. Influence of strain rate and strain at temperature on TRIP effect in a metastable austenitic stainless steel. Mater Sci Eng, A 2020;777:139046.
[20] Ganesh BJ, Raju S, Rai AK, Mohandas E, Vijayalakshmi M, Rao KBS, Raj B. Differential scanning calorimetry study of diffusional and martensitic phase transformations in some 9 wt-%Cr low carbon ferritic steels. Mater Sci Technol 2011;27(2):500–12.
[21] Gu C, Bassim N, Zurob H. In-situ study of microstructure in phase transformation of pipe line steel. Microsc Microanal 2021;27:1554–5.
[22] Zhao S, Wei DL, Li RB, Zhang L. Effect of cooling rate on phase transformation and microstructure of NbTi microalloyed steel. Mater Trans 2014;55:274–1279.
[23] Xu G, Wan L, Yu SF, Liu L, Luo F. A new method for accurate plotting continuous cooling transformation curves. Mater Lett 2008;62:3978–80.
[24] Kawuloková M, Smetana B, Zlá S, Kalup A, Mazancová E, Váňová P, Kawulok P, Dobrovská J, Rosypalová S. Study of equilibrium and nonequilibrium phase transformations temperatures of steel by thermal analysis methods. J Therm Anal Calorimetry 2017;127:423–9.
[25] Rowolt C, Milkereit B, Springer A, Kreyenschulte C, Kessler O. Dissolution and precipitation of copper-rich phases during heating and cooling of precipitation-hardening steel X5CrNiCuNb16-4 (17-4 PH). J Mater Sci 2020;55:13244–57.
[26] Bernhard M, Fuchs N, Presoly P, Angerer P, Friessnegger BBC. Characterization of the γ-loop in the Fe-P system by coupling DSC and HT-LSCM with complementary in-situ experimental techniques. Mater Char 2021;174:111030.
[27] Mu W, Shibata H, Hedström P, Jönsson PG, Nakajima K. Combination of in-situ microscopy and calorimetry to study austenite decomposition in inclusion engineered steels. Steel Res Int 2015;87:10–4.

[28] Liu H, Du C, Lan P, Tang H, Shang C, Zhang J. Simultaneous formation of inter- and intragranular ferrite in microalloyed steels studied by modeling and experiment. Mater Sci Technol 2017;114:401.
[29] Wu SW, Zhang CJ, Zhu LG, Zhang QJ, Ma XG. In-depth analysis of intragranular acicular ferrite three-dimensional morphology. Scripta Mater 2020;185:61–5.
[30] Bernhard M, Presoly P, Fuchs N, Bernhard C, Kang YB. Experimental study of high temperature phase equilibria in the iron-rich part of the Fe-P and Fe-C-P systems. Metall Mater Trans A 2020;51:5351–64.
[31] Bernhard M, Presoly P, Bernhard C, Hahn S, Ilie S. An assessment of analytical liquidus equations for Fe-C-Si-Mn-Al-P-alloyed steels using DSC/DTA techniques. Metall Mater Trans B 2021;52:2821–30.
[32] Boettinger WJ, Kattner UR, Moon KW, Perepezko JH. DTA and heat-flux DSC measurements of alloy melting and freezing. NIST Recommended Practice Guide; 2006. *Special Publication 960-15*.
[33] Reid M, Phelan D, Dippenaar R. Concentric solidification for high temperature laser scanning confocal microscopy. ISIJ Int 2004;44(3):565–72.
[34] Griesser S, Dippenaar R. Enhanced concentric solidification technique for high-temperature laser-scanning confocal microscopy. ISIJ Int 2014;54(3):533–5.
[35] Fuchs N, Krajewski P, Bernhard C. In-situ observation of austenite grain growth in plain carbon steels by means of high-temperature laser scanning confocal microscopy. Berg- und Huettenmaennische Monatshefte 2015;160:214–20.
[36] Fuchs N, Bernhard C. Potential and limitations of direct austenite grain growth measurement by means of HT-LSCM. Mater Today Commun 2021;28:102468.
[37] Garcia de Andres C, Caballero FG, Capdevila C, San Martin D. Revealing austenite grain boundaries by thermal etching: advantages and disadvantages. Mater Char 2002;49(2):121–7.
[38] Kern M, Bernhard M, Bernhard C, Kang Y-B. Grain boundary mobility of $\gamma$-Fe in high-purity iron during isothermal annealing. Scripta Materialia 2023;230:115431.
[39] Saunders N, Guo Z, Li X, Miodownik AP, Schillé JP. The calculation of TTT and CCT diagrams for general steels. Sente Software Ltd; 2004.